sciendo

Nordic Concrete Federation

© Article authors. This is an open access article distributed under the Creative Commons Attribution-NonCommercial-NoDerivs licens. (http://creaticecommons.org/licenses/by.nc-nd/3.0/).

ISSN online 2545-2819
ISSN print 0800-6377

DOI: 10.2478/ncr-2021-0019

Received: Oct. 31, 2021
Revision received: Dec. 23, 2021
Accepted: Dec. 27, 2021

Numerical Modelling of Heat Transport in Freezing Mortars with an External Liquid Reservoir

Abdul Faheem, M.Sc.
Ph.D. Student
DTU Civil Engineering, Technical University of Denmark
Brovej Building 118, 2800 Kgs. Lyngby, Denmark
abfah@byg.dtu.dk

Maxime Ranger, M.Sc.
Industrial Ph.D. student
Danish Road Directorate and
DTU Civil Engineering, Technical University of Denmark
Guldalderen 12, 2640 Hedehusene, Denmark
maxr@vd.dk

Marianne Tange Hasholt, Ph.D.
Associate Professor
DTU Civil Engineering, Technical University of Denmark
Brovej Building 118, 2800 Kgs. Lyngby, Denmark
matah@byg.dtu.dk

ABSTRACT
Several studies indicate that the temperature distribution in concrete may affect the extent of frost scaling. This study presents a numerical model that describes the thermal response of freezing mortars in the presence of an external liquid reservoir, where the external liquid is either pure water or 3% sodium chloride solution. The phase transformation of supercooled external liquid is modelled in two stages: quick freezing, when the supercooled liquid starts to form crystals and slow freezing. The model is developed in two parts. In part I, the focus is the modelling of external liquid, and therefore a non-porous body with an external liquid reservoir is modelled and validated. In part II, the model developed in part I is developed further for a porous body containing different phases, i.e., unfrozen liquid and ice, in the pores. A comparison of simulated and experimentally measured temperature distributions shows a good agreement.

Key words: Freezing and thawing, temperature distribution, heat transport, numerical modelling

1. INTRODUCTION

Freeze-thaw resistance of concrete is a durability concern in cold climates. Concrete structures exposed to freezing and thawing cycles may show surface scaling and internal cracking. During wintertime, deicing chemicals are used, e.g. to ensure the uninterrupted traffic flow on concrete roads and bridges. As a result, a liquid solution forms on the concrete surface. The solution may not completely freeze while the environmental temperature fluctuates above and below the freezing point. The deicing chemicals in the liquid are known to increase frost scaling [1].

Several theories attempt to describe the freeze-thaw damage mechanism (see [2] for an overview), but the mechanism of freeze-thaw damage is still not completely understood. Many theories propose that ice formation in pores and associated actions cause freeze-thaw damage. Therefore, it is believed that the coupled action of heat and moisture transport in concrete is the primary source of damage during freeze-thaw action, both in terms of internal cracking and surface scaling. Since the ice formation is strongly dependent on temperature, the temperature distribution in concrete can influence the ice formation in pores and associated moisture movements. The temperature distribution becomes even more important when unfrozen liquid is present on one or more surfaces as, in certain cases, the external liquid can be transported to freezing concrete. A few examples in the literature indicate that the temperature distributions in the concrete may change the extent of frost scaling [3–7]. However, the effects of temperature distribution are rarely studied in relation to frost scaling. Numerical models providing temperature distribution in freezing concrete can help to understand the relationship between the temperature distribution and frost scaling and thereby improve the understanding of the freeze-thaw damage mechanism.

Several models in the literature attempt to describe the freezing behaviour of cement-based materials containing pure water in pores [8–12] and provide firm knowledge of the modelling of freeze-thaw action. However, they are limited to the case where there is no external liquid. A few models consider the presence of external liquid [12,13], but the supercooling of external liquid is not considered. Phase transformation of supercooled liquid is an important yet ignored aspect during freeze-thaw action. Generally, the more supercooling, the higher the ice formation rate and heat release rate will be. Several existing models consider the freezing point depression of liquid due to dissolved substances but do not consider supercooling. Esmaeeli et al. [14] considered the phase transformation within pores with supercooling effect, yet without an external liquid reservoir.

The aim of this study is to develop a model that describes the thermal response of mortar containing different phases in pores when one of the mortar surfaces is in contact with an external liquid reservoir. Moreover, it is also the aim to model phase transformation of liquid to ice considering the supercooling effect. The model is developed in two parts using COMSOL Multiphysics. In part I, the thermal response of a non-porous body is modelled, as the focus of this part is the modelling of external liquid. In part II, the model developed in part I is further developed to represent a porous body like mortar. The model is also validated in two parts. Part I is validated using experimental observations made on a polyoxymethylene (POM) specimen, while part II is validated using experimental observations obtained with mortar specimens. The model can be used to study the influence of salt concentration, external liquid thickness, and surrounding temperature on temperature distribution in freezing mortars.

2. THEORY

2.1 The freezing process

The understanding of freeze-thaw action requires knowledge of the freezing process. When a liquid contains dissolved substances or experiences pressure change, e.g., due to surface tension in the interface of phases existing in small pores, its freezing point is affected. If these factors decrease the freezing point of the liquid, it is referred to as the freezing point depression. In a liquid that is subject to freezing, several ice nuclei develop and then melt due to unfavourable energy circumstances and lack of the phenomenon known as suitable disturbance [15]. Ice formation requires critical size nuclei that, instead of melting, continue to attract molecules to form small clusters. In favourable energy circumstances, liquid molecules and small clusters arrange themselves in a configuration that characterizes the liquid's transformed solid phase (e.g. ice for water). Due to the absence of critical size nuclei, liquids frequently remain unfrozen below their freezing point. This is called supercooling (also known as undercooling), and the liquid that remains unfrozen below its freezing point is termed as a supercooled liquid [15]. The pure bulk water begins to supercool below 0°C, while a 3% sodium chloride (NaCl) solution begins to supercool below approx. -1.9°C, as 0°C and -1.9°C are the freezing points of pure bulk water and 3% NaCl solution, respectively.

2.2 Freezing peak

When ice formation starts in a supercooled liquid, substantial latent heat of fusion is released in a very short period causing a sudden rise in temperature (recalescence) of the body transforming from liquid to ice. Figure 1(a) shows a typical freezing peak that appears when a supercooled liquid transforms to ice during a typical temperature cycle used for the freeze-thaw test (see [16]). Figure 1(b) shows a schematic representation of different parts of the freezing peak. The ice formation process in supercooled liquid can be modelled in two stages: the recalescence stage and the slow freezing stage. In the recalescence stage, the ice nuclei grow rapidly in the form of dendritic ice, whereas in the slow freezing stage, ice crystals grow slowly as they do when a bulk liquid starts freezing without supercooling [17]. The former stage depends on the extent of supercooling, whereas the latter stage depends on how quickly the latent heat of fusion is removed.

At the start of the freezing peak (indicating the start of ice formation), the temperature curve starts to rise and reaches the top of the freezing peak. This is a temperature at which different phases (unfrozen liquid and ice) are in thermodynamic equilibrium, which is often the melting point.

After reaching the top temperature, the thermodynamic equilibrium is maintained, where the transforming body remains at the same (or likewise) temperature until all the liquid that can freeze during the freezing peak has frozen. The time period taken by the plateau reflects this freezing. After that, the temperature curve decelerates and eventually attains a likewise slope (or the same slope in an ideal case) as before the start of the freezing peak. The shape of the freezing peak can differ depending on the extent of supercooling and the composition of the transforming liquid. For example, after the peak top, the plateau of the curve either narrows down or disappears if the liquid is 3% NaCl solution. The width of the freezing peak can be determined by the difference between the peak start and the peak end times.

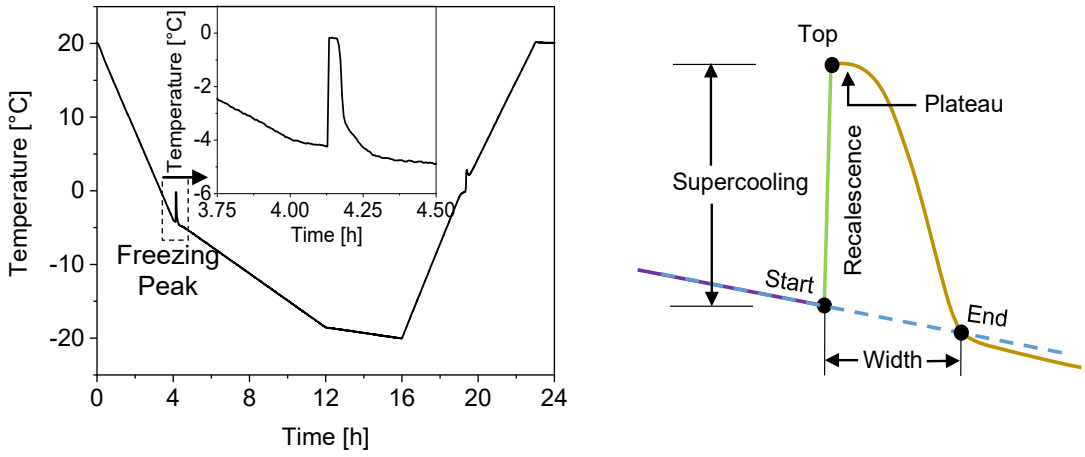

Figure 1 – Freezing peak occurring in supercooled liquid: (a) A typical freezing peak observed when freezing pure water, (b) Schematic representation of the freezing peak and its parts.

3. PART I: EXTERNAL LIQUID FREEZING WITH NON-POROUS BODY

In part I, the freezing process of external liquid is modelled when it is retained on the surface of the POM specimen, a non-porous medium that neither contains pore liquid nor changes its thermal properties. The POM specimen was used to avoid the effect of liquid freezing in pores on thermal response. The energy balance is used to describe heat transport, neglecting energy dissipation and convective heat transport. The phase transformation of external liquid is modelled through modifications in heat capacity, and supercooling is modelled using an artificial heat source. The temperature dependent thermal properties of the external liquid are incorporated according to the altering state of the liquid (unfrozen, mushy, solid).

3.1 Model geometry and temperature boundaries

Figure 2(a) shows the schematic representation of the model geometry and location of points where the temperature is examined. The goal is to model a standard freeze/thaw test setup (CEN/TS 12390-9 [16]), where a rubber sheet and thermal insulation is placed on a 50 mm thick specimen (except the test surface). Therefore, the modelled geometry includes a 2D axisymmetric circular body of 44.625 mm radius, rubber sheet and thermal insulation, and a layer of external liquid on top of the specimen, as suggested in the standard (see Figure 2(a)). Figure 2(a) also shows the temperature boundary designed on the external liquid surface to apply freeze-thaw cycle (FTC), whereas the applied FTC (setpoints) is shown in Figure 2(b). A temperature gradient

exists in the external liquid, and therefore the temperature boundary at the external liquid surface is adjusted in such a way that the points marked on FTC in Figure 2(b) are obtained at the test surface. The surrounding temperature is also specified at the edges of the modelled setup (Figure 2(a)).

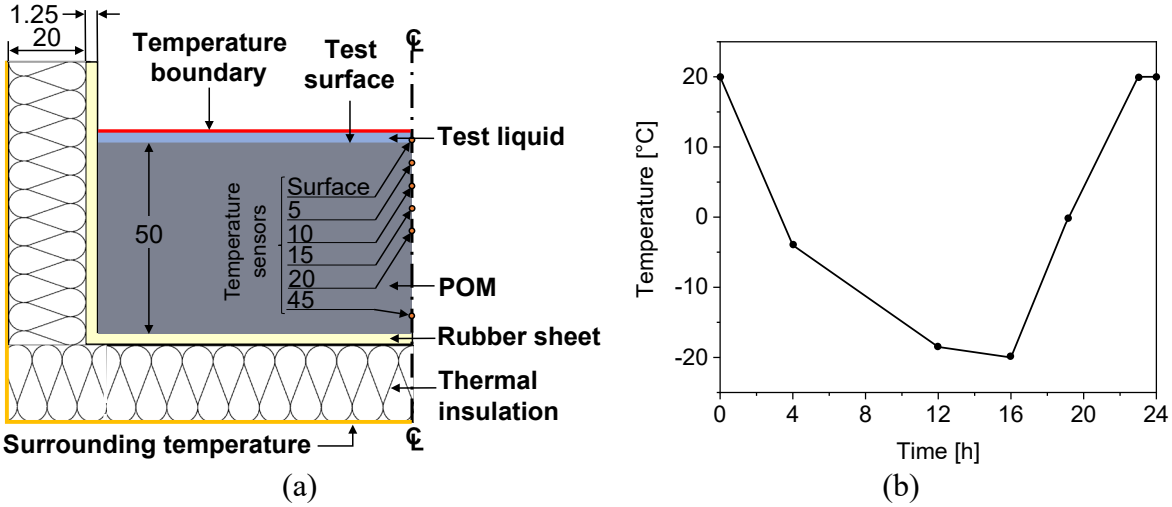

Figure 2 – (a) Cross-section of the modelled test setup with temperature sensor locations relative to the test surface (unit: [mm])*, (b) Freeze-thaw cycle applied on the test surface.*

3.2 Modelling of external liquid

The energy balance of the external liquid is obtained using the heat equation as:

$$\rho_{\in} C_{\in} \frac{\partial T}{\partial t} - \nabla[k_{\in} \nabla T] = Q_{\in} \tag{1}$$

where t is time [s], T is the temperature [K], and $\in$ indicates the composition of the external liquid (e.g. pure water by "dw" and 3% NaCl solution by "sol"). $\rho_{\in}$, $C_{\in}$, and $k_{\in}$ are the density [kg/m^3], the specific heat capacity [J/(g.K)], and the thermal conductivity [W/(m.K)] of the external liquid with composition $\in$, respectively. $Q_{\in}$ takes into account the latent heat of fusion [W/m^3] during the recalescence stage and otherwise remains zero. How $Q_{\in}$ is used to model supercooling, and the recalescence stage are described in the section “Supercooling and phase change”.

Volume fractions and thermal properties of external liquid
When phase transformation of pure water takes place, it transforms completely into ice during the freezing peak. Theoretically, the properties of pure water change to the properties of ice within an infinitely small temperature change. Such a sudden change in thermal properties and volume fractions causes computational issues. Therefore, a logistic function that ensures the start of phase transformation at 0°C and its end at -1°C is used. The volume fractions of unfrozen pure water $n_{\mathrm{dw,l}}$ [-] and the ice that transforms from pure water $n_{\mathrm{dw,i}}$ [-] are obtained as:

$$n_{\mathrm{dw,l}} = \frac{1}{1 + \mathrm{e}^{-20(T+0.5)}}$$
$$n_{\mathrm{dw,i}} = 1 - n_{\mathrm{dw,l}} \tag{2}$$

where T is in [°C] (the program automatically obtained consistent units). The subscripts i and l

indicate ice and unfrozen liquid, respectively. In case of 3% NaCl solution, part of the solution remains unfrozen after the freezing peak, and its freezing depends on the temperature and NaCl concentration. A lever rule is used to describe the freezing of the 3% NaCl solution, as [18]:

$$T_{\mathrm{m,sol}} = -0.59484c_{\mathrm{s}} - 0.00058275{c_{\mathrm{s}}}^2 - 0.0005436{c_{\mathrm{s}}}^3 \tag{3}$$

where $T_{\mathrm{m,sol}}$ is the melting temperature of the solution [°C] and c_{s} is the temperature dependent NaCl concentration in the freezing solution [%]. The volume fractions of ice that transforms from 3% NaCl solution $n_{\mathrm{sol,i}}$ [-] and unfrozen NaCl solution $n_{\mathrm{sol,l}}$ [-] are obtained as:

$$\begin{aligned} n_{\mathrm{sol,i}} &= 1 - \frac{c_0}{c_{\mathrm{s}}} \\ n_{\mathrm{sol,l}} &= 1 - n_{\mathrm{sol,i}} \end{aligned} \tag{4}$$

where c_0 is the initial NaCl concentration [%] above its liquidus line. The combination of Eqs. (3) and (4) provides $T_{\mathrm{m,sol}}$ and $n_{\mathrm{sol,i}}$ when c_{s} values are varied and a constant c_0 is provided. The unfrozen external liquid is assumed to have constant properties shown in Table 1, whereas its properties become a mix of these properties after the start of ice formation.

Table 1 – Thermal properties of the external liquid in different states

Material	ρ [kg/m^3]	C [J/(g.K)]	k [W/(m.K)]
Ice [18]	917	2.030	2.25
Pure water or NaCl solution [19]	997	4.121	0.5886

The phase transformation of liquid into ice in the slow freezing stage is primarily modelled through modifications in the specific heat capacity of the external liquid (C_ϵ) according to the apparent heat capacity method (see e.g. [20]):

$$\begin{aligned} C_\epsilon &= C_{\mathrm{pc}} + C_{\mathrm{fp}} = \left[\frac{\rho_{\epsilon,\mathrm{i}} n_{\epsilon,\mathrm{i}} C_{\epsilon,\mathrm{i}} + \rho_{\epsilon,\mathrm{l}} n_{\epsilon,\mathrm{l}} C_{\epsilon,\mathrm{l}}}{\rho_{\epsilon,\mathrm{i}} n_{\epsilon,\mathrm{i}} + \rho_{\epsilon,\mathrm{l}} n_{\epsilon,\mathrm{l}}}\right] + \left[\Delta H \frac{d\alpha_{\mathrm{m}}}{dT}\right] \\ \alpha_{\mathrm{m}} &= \frac{1}{2}\frac{\rho_{\epsilon,\mathrm{l}} n_{\epsilon,\mathrm{l}} - \rho_{\epsilon,\mathrm{i}} n_{\epsilon,\mathrm{i}}}{\rho_{\epsilon,\mathrm{l}} n_{\epsilon,\mathrm{l}} + \rho_{\epsilon,\mathrm{i}} n_{\epsilon,\mathrm{i}}} \end{aligned} \tag{5}$$

where C_{pc} [J/(g.K)] describes the variation in C_ϵ due to phase transformation for the entire freezing/thawing cycle, and C_{fp} [J/(g.K)] takes into account latent heat of fusion and modifies C_ϵ below the melting point. ΔH is the heat of fusion of ice [kJ/kg]. $n_{\epsilon,\mathrm{i}}$ is obtained using Eq. (2) when external liquid is pure water and a combination of Eqs. (3) and (4) when it is 3% NaCl solution. As a logistic function is used to avoid computational issues for pure water, a moving average is used to smoothen the C_{fp} curves to avoid the computational issues.

The density of external liquid (ρ_ϵ) is obtained by calculating the weighted average of ice and unfrozen liquid, as:

$$\rho_\epsilon = \rho_{\epsilon,\mathrm{i}} n_{\epsilon,\mathrm{i}} + \rho_{\epsilon,\mathrm{l}} n_{\epsilon,\mathrm{l}} \tag{6}$$

Thermal conductivity of the external liquid (k_ϵ) is obtained using the modified Maxwell-Eucken

model, as [21]:

$$
\begin{aligned}
k_{\in} &= \frac{(2\Lambda+1)-2(\Lambda-1)F_{\mathrm{b}}}{(2\Lambda+1)+(\Lambda+1)F_{\mathrm{b}}} \\
\Lambda &= \frac{k_{\in,\mathrm{i}}}{k_{\in,\mathrm{l}}} \\
F_{\mathrm{b}} &= \frac{1}{2}\left[\left(\frac{2}{\varrho}-1+2n_{\in,\mathrm{l}}\right)-\sqrt{\left(\frac{2}{\varrho}-1+2n_{\in,\mathrm{l}}\right)^{2}-\left(\frac{8}{\varrho}\right)n_{\in,\mathrm{l}}}\right] \\
\varrho &= \frac{(\Lambda-1)^{2}}{(\Lambda+1)^{2}+0.5\Lambda}
\end{aligned}
\tag{7}
$$

where Λ is the ratio of thermal conductivities of the ice and the liquid phases, ϱ is a function of Λ as defined above, and F_{b} is a function of ϱ and $n_{\in,\mathrm{l}}$ as defined above.

Supercooling and phase change

The experimentally measured temperature of the start of ice formation at the test surface $T_{\mathrm{sup},\in}$ is used to consider the supercooling of external liquid [°C]. $T_{\mathrm{sup},\in}$ is shown as "Peak start" temperature in Table 3. Events interface in COMSOL is used to model the freezing stages, where the temperature predicted by the model at the test surface T_{s} is used to define the start and the end of the events [°C]. An artificial heat source is generated to take into account $Q_{\in}$ for the recalescence stage, whereas modifications in thermal properties (primarily $C_{\in}$) are used to model the slow freezing stage. The description of the freezing stages and events are as follows:

- When $T_{\mathrm{s}} > T_{\mathrm{sup},\in}$, the specific heat capacity, the thermal conductivity, and the density of the external liquid are as of its liquid phase (Table 1).
- When $T_{\mathrm{s}} = T_{\mathrm{sup},\in}$, an artificial heat source turns on and heats the liquid, marking the start of the recalescence stage. The rate of the heat release is defined by $Q_{\in}$ (see below). In general, $Q_{\in}$ is adjusted to accommodate computational limitations, so that the temperature curve reaches peak top quickly yet not exceeding much the melting point to mimic the recalescence stage of supercooled liquid.
- When T_{s} reaches the melting point of the bulk external liquid $T_{\in,m}$ [°C], the artificial heat source turns off, and the slow freezing stage starts.
- In the slow freezing stage, specific heat capacity, density, and thermal conductivity of the external liquid are obtained using Eq. (5), Eq. (6), and Eq.(7), respectively. The modified thermal properties consider latent heat related to this stage; no heat source is involved in the slow freezing stage.
- After having the plateau during the slow freezing stage, the temperature curve decelerates under the effect of applied temperature.

Stefan number equals the product of specific heat capacity and degree of supercooling divided by the latent heat of fusion. It has been used to calculate the amount of ice formed during the recalescence stage [17]. However, it is challenging to define the rate of dendritic ice growth to calculate $Q_{\in}$. Shaolei et al. [17] stated that different speeds of dendritic ice growth cause a marginal difference in simulation results. It was therefore attempted to define $Q_{\in}$ by using the following approaches:

- Calculating the Stefan number and assuming different rates of ice growth

- Adjusting the value of $Q_{\in}$ with the time step by trials and adopting a suitable value that ensures that the required sudden rise in temperature (recalescence) is obtained, while the solver catches the $T_{\in,\mathrm{m}}$ and does not exceed it too much.

The freezing peaks obtained with these methods showed marginal differences. The first-mentioned method took more time to solve. Therefore, the latter method is adopted for simplicity.

3.3 Energy balance for POM specimen

The energy balance for the POM specimen is obtained using the heat equation, as:

$$\rho_{\mathrm{pom}} C_{\mathrm{pom}} \frac{\partial T}{\partial t} - \nabla\left[k_{\mathrm{pom}} \nabla T\right] = 0 \tag{8}$$

where ρ_{pom}, C_{pom}, and k_{pom} are the density [kg/m^3], the specific heat capacity [J/(g.K)], and the thermal conductivity [W/(m.K)] of the POM specimen, respectively. Since phase transformation does not take place in the POM specimen, its properties remain constant during the FTC.

Table 2 provides experimentally measured thermal properties of POM and other materials shown in Figure 2(a) except the external liquid. The thermal conductivity and thermal effusivity of each material were measured using TCi thermal conductivity analyzer that conforms to ASTM D7984, D5334, and D5930 (see [22] for the equipment details and description of the test procedure for different materials). The heat capacity was then calculated using the density (manufacturer provided) and measured thermal conductivity and thermal effusivity of the material.

Table 2 – Thermal properties of POM, rubber sheet, and thermal insulation

Material	ρ [kg/m^3]	C [J/(g.K)]	k [W/(m.K)]
POM	1384	1.120	0.46
Rubber sheet with glue	1550	1.050	0.61
Thermal Insulation	50	2.400	0.038

3.4 Validation of Part I

The reference method of CEN/TS 12390-9 (Borås method) [16], where the temperature of the test liquid is controlled, was the starting point. The setup consisted of a test specimen, a temperature control unit, and a climate chamber. The schematic representation in Figure 2(a) is also the schematic representation of the experimental setup except the temperature boundary (red line) that was replaced by a temperature control unit. The temperature distribution was measured using calibrated type T thermocouples.

Geometry of POM specimen

The shape and the dimensions of the POM specimen were the same as those of the mortar specimens (Figure 5). Though the shape of the POM specimen (also mortar specimens) was different from the shape of the modelled test specimen (circular) to simplify the model and reduce the computational cost, the insulated surface area of the POM specimen (also mortar specimens) was identical to the modelled test specimen. Thermocouples were inserted in the holes drilled in

the POM specimen at specified locations (Figure 2(a)). A rubber sheet was glued, and thermal insulation was placed on specimen surfaces except the test surface (see [16]).

Temperature boundary conditions
A Peltier element based temperature control unit was used to apply freeze-thaw cycles on the test surface. The Peltier element applied cooling, whereas a built-in heating element was used to apply heating. A 20 mm thick aluminium plate was attached to the unit where the shape of the aluminium plate was similar to the geometry of the test surface (Figure 5) with slightly smaller dimensions (reduced by an offset of 5 mm). A LabVIEW program that included a PID control algorithm was used to control the response of the temperature control unit, based on input from a type T thermocouple hanging in the external liquid (sensor location was not well defined). This sensor updated the temperature every second. Identical PID values were used for all experiments.

The thickness of the external liquid was maintained using spacers of specific heights. The aluminium plate and test liquid were in contact. After placing the temperature control unit on the test surface, the setup was placed in a programmable climate chamber. The climate chamber was used to control the surrounding temperature of the setup. A type T thermocouple was used to measure and feedback the air temperature of the climate chamber.

Table 3 shows the four conducted experiments and the features of the corresponding freezing peaks measured experimentally. The experiment ID reflects levels of the variables considered in the experiment. For example, the experiment ID "POM-0s-3mm-20°C" reflects that it is a POM specimen, the salt concentration in the external liquid is 0%, the external liquid layer thickness is 3 mm, and the surrounding temperature is 20°C.

Table 3 – Overview of validation experiments conducted with POM specimens including experimentally measured features of the corresponding freezing peaks

Expeiment ID	NaCl concentration [%]	Liquid layer thickness [mm]	Peak start* ($T_{\sup,\in}$) [°C]	Peak top* ($T_{\in,m}$) [°C]
POM-0s-3mm-20°C	0	3	-2.634	-0.084
POM-3s-3mm-20°C	3	3	-3.348	-1.920
POM-0s-7mm-20°C	0	7	-3.246	-0.084
POM-3s-7mm-20°C	3	7	-3.144	-1.614

* Section 2.4 describes how peak start and peak top are defined

3.5 Results and discussion of non-porous body

Development of temperature distribution
Figure 3 compares simulated (solid lines) and experimentally measured (dotted lines) development of temperature distribution in the POM specimen considering the boundary conditions provided in Table 3. The data set providing temperature distribution data for seven freeze-thaw cycles for each experiment in Table 3 can be accessed in Ref. [23]. Generally, the simulation results show a good agreement with the experimental results. However, there are some differences in comparison to the experimental results. The results show that there is an offset between the simulated temperature curves and the corresponding experimentally measured temperature curves at different depths. The location of temperature sensing points is well defined

in the simulation, whereas a temperature sensor may not be located at the defined location in the experiments, and possible dislocation of the sensor can cause the observed discrepancies.

The difference in the geometry of the modelled specimen (see Section 3.1) and the specimen used in experiments (Figure 5) can add to the observed temperature offset. A model where the specimen geometry shown in Figure 5 was modelled demonstrated a better agreement (results are not shown).

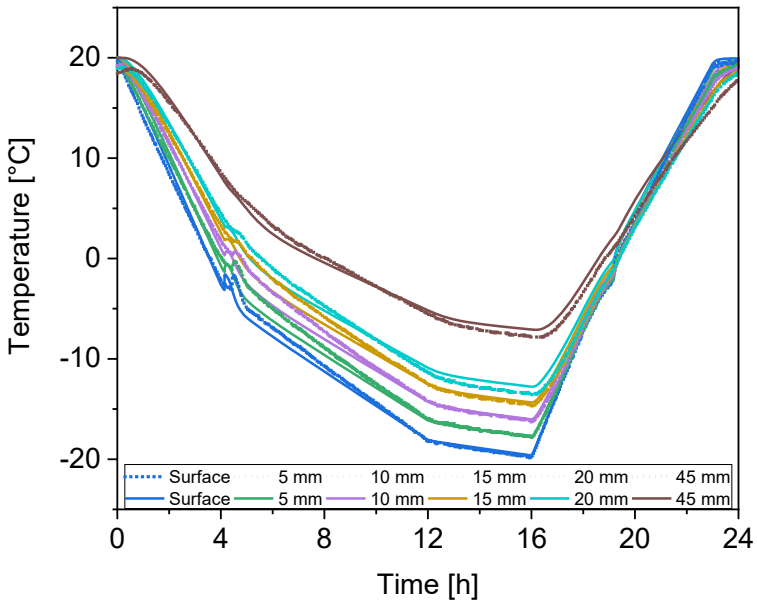

Figure 3 – Comparison of a typical temperature distribution obtained from simulations (solid lines) and experiments (dotted lines) for POM specimen (obtained from POM-3s-7mm-20°C).

The temperature offset is pronounced in the region of phase transformations (both during freezing and thawing). Especially, a high temperature offset appears in simulated curves after the freezing peak where the temperature curve does not follow the same path as before the freezing curve but rather becomes lowered until the surface temperature reaches -18.5°C. This can be a consequence of inaccurate modelling of the thermal properties of the external liquid. For example, if the Maxwell-Eucken model is predicting a thermal conductivity that is too high, then the heat transport is faster, and thus the surface can become colder more quickly than it happens in reality.

In addition, the way the freeze/thaw cycle is applied in simulations can cause such discrepancies. A PID control algorithm controlled the response of the temperature control unit in experiments. The temperature control unit was able to apply heating/cooling according to the difference between the setpoint and the feedback temperature. This temperature difference was the largest during the phase transformation events. Here, the temperature control unit used its full capacity to reach the setpoint. However, a defined freeze/thaw cycle was applied in simulations, and additional heating/cooling was not applied during phase change events. As a result, the temperature offset remained present until the surface temperature reached -18.5°C. During thawing, the simulated temperature curves remain at the melting point for a longer period than the experimental temperature curves, where this effect was more obvious for pure water. This is also the consequence of not considering additional heating/cooling in simulations. Section 4.5 provides the experimental observations to support the presented arguments.

Analysis of freezing peaks

The freezing peaks are enlarged in Figure 4 to demonstrate how well the simulated freezing peaks (solid lines) agree with the experimental freezing peaks (dotted lines). The start and the top of the simulated freezing peaks match well with the experimental freezing peaks due to the fact that the heat source was turned on and off, considering the same temperatures. The start of the freezing peak shows a good agreement in terms of temperature but shows a slight difference in terms of time due to the temperature offset between the simulation and experimental temperature curves.

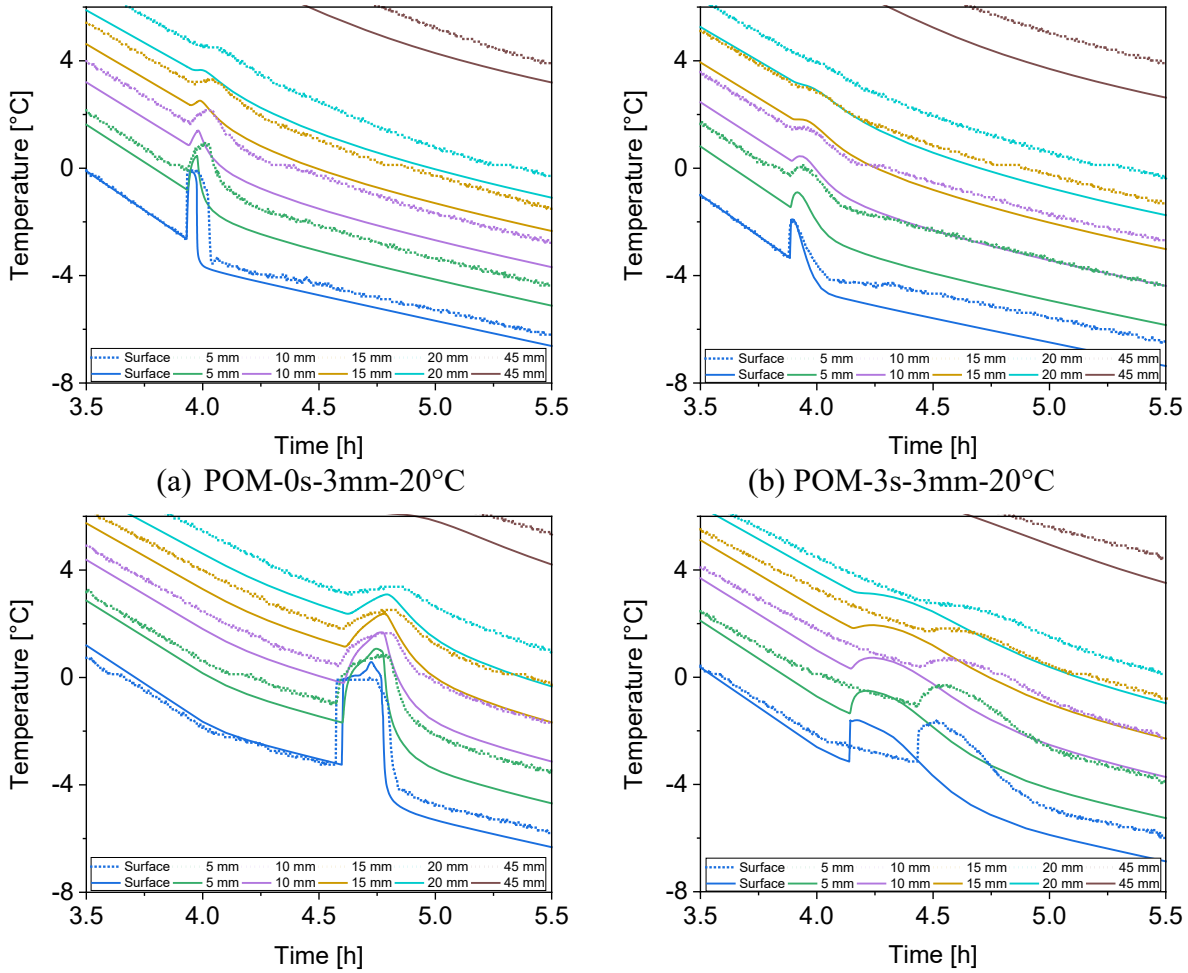

Figure 4 – Comparison of the freezing peaks obtained from simulations (solid lines) and experiments (dotted lines) for experiments with POM specimen.

The width of the simulated freezing peaks is generally narrower than the experimental freezing peaks. The maximum power of the temperature control unit was limited, whereas the simulated temperature boundary had infinite power. As a result, it took longer to remove the latent heat in experiments compared to the simulations. The simulation of the freezing peak of 7 mm thick pure water (Figure 4(c)) shows an odd behaviour. After reaching the peak top ($T_{\in,m}$), the temperature curve rises and exceeds the melting point (0°C), which is physically incorrect. Since only the thickness of the external liquid layer was changed for this simulation, this is probably a computational error.

Figure 4 also shows the influence of salt concentration of the external liquid on freezing peaks

when Figures 4 (a) and (c) are compared with Figures 4 (b) and (d), respectively. It shows that the plateau of the freezing peak is wider when the 3mm thick external liquid is pure water (Figure 4 (a)) compared to when it is 3% NaCl solution (Figure 4(b)). As mentioned in Section 3.2, supercooled pure water freezes completely during the freezing peak, whereas the entire 3% NaCl solution does not freeze during the freezing peak. According to the lever rule (Eq. (3)), approx. 21% volume of an initially 3% NaCl solution remains unfrozen at -10°C. Therefore, more volume of pure water freezing during the freezing peak results in a wider plateau than for a 3% NaCl solution. This observation shall also be true for 7mm thick external liquid, but it is not truly reflected when Figure 4(c) is compared with Figure 4(d). The experimental freezing peak in Figure 4(d) does not quickly reach the peak top. Instead, it rises slowly after a certain level of sudden rise. In the present experimental setup, ice formation probably started at the liquid surface (coldest place at peak start), and the temperature recorded at the test surface was the effect of heat transport from the freezing site. An additional temperature sensor was placed in the middle of the 7 mm thick external liquid to observe the temperature development relatively closer to the freezing site. The obtained temperature curves verified that the plateau for pure water was longer than the plateau for the 3% NaCl solution (results not shown).

Moreover, Figure 4 shows the influence of the external liquid layer thickness on the freezing peaks when Figures 4 (a) and (b) are compared to Figures 4 (c) and (d), respectively. The width of the freezing peaks increases when the external liquid layer thickness is increased. This increase in width can be attributed to the additional volume of 7 mm thick external liquid freezing during the freezing peak. The results show that the simulated freezing peaks seem to capture the effect of the salt concentration and the thickness of the external liquid layer observed in the experiments.

4. PART II: MODELING OF POROUS BODY

In part II, the model developed in part I is developed further, as the non-porous POM is replaced with mortar. The developed model and other relevant files can be accessed in Ref. [24]. The mortar is modelled as a multiphase porous medium consisting of solid and pore space defined as total porosity n. The amount of freezing liquid in pores is negligible compared to the amount of freezing external liquid at a specific freezing temperature, and the assumption regarding pore saturation has a marginal effect on heat transport. Therefore, the mortar is assumed to be fully saturated with water. The pore space contains pore liquid (pl) and pore ice (pi) depending on the temperature. The energy balance for mortar can be expressed as:

$$\rho_{\mathrm{m}} C_{\mathrm{m}} \frac{\partial T}{\partial t} - \nabla[k_{\mathrm{m}} \nabla T] = 0 \tag{9}$$

where ρ_{m}, C_{m}, and k_{m} are the density [kg/m^3], the specific heat capacity [J/(g.K)], and the thermal conductivity [W/(m.K)] of mortar, respectively. The latent heat associated with pore liquid freezing is considered while determining C_{m}. It is assumed that the supercooling of the pore liquid is equivalent to the supercooling of the external liquid. Therefore, ice formation in the external liquid and in the pore liquid starts simultaneously.

4.1 Volume fractions of phases in mortar

The solid part in the mortar can be separated as cement paste and fine aggregates, where the cement paste consists of unhydrated cement, gel solid, and gel and capillary water. The volume

fractions of these phases in the cement paste are calculated using Power's model [25,26]. For calculations, it is considered that the water to cement ratio is 0.45, cement to sand ratio is 0.33, the density of cement is 3140 kg/m^3, the density of sand is 2640 kg/m^3, and the degree of hydration is 0.75. The volume fraction of freezable pore liquid $n_{\mathrm{fpl,m}}$ is obtained as 0.09, the volume fraction of cement (unhydrated and hydrated) including gel water $n_{\mathrm{cem,m}}$ is obtained as 0.31, and the volume fraction of sand $n_{\mathrm{snd,m}}$ is obtained as 0.60, with respect to the mortar volume. Since mortar is assumed fully saturated, $n_{\mathrm{fpl,m}}$ equals n. The mass fractions of freezeable pore liquid $w_{\mathrm{fpl,m}}$, cement (unhydrated and hydrated) including gel water $w_{\mathrm{cem,m}}$, and sand $w_{\mathrm{snd,m}}$ are obtained as 0.04, 0.28, and 0.68, respectively, with respect to the mortar mass.

4.2 Ice formation in pores

It is seldom that homogenous ice nucleation occurs in a porous medium. The ice forms in large pores and propagates into small connected pores. The van Genuchten equation can be used to estimate the degrees of ice saturation S_{pi} [-] and liquid saturation S_{pl} [-] in mortar [27]:

$$S_{\mathrm{pi}} = 1 - S_{\mathrm{pl}}$$
$$S_{\mathrm{pl}} = S_\delta + (1 - S_\delta)\left[1 + \left(\frac{-\Delta\mathcal{S}_{\mathrm{fv}}(T - T_{\mathrm{m,p}})}{\mathcal{N}}\right)^{\frac{1}{1-m}}\right]^{-m} \tag{10}$$

where $\Delta\mathcal{S}_{\mathrm{fv}} = 1.2227$ MPa/K is the melting entropy of ice, $S_\delta = 0.085$ is the degree of saturation of the liquid-like layer adsorbed on pore walls that remains unfrozen during the freezing process, and $m = 0.41$ and $\mathcal{N} = 0.45$ MPa are constants associated to pore structure [27]. Since the relations of the degree of saturation are $S_{\mathrm{pi}} = n_{\mathrm{pi}} / n_{\mathrm{fpl,m}}$ and $S_{\mathrm{pl}} = n_{\mathrm{pl}} / n_{\mathrm{fpl,m}}$, the volume fraction of pore ice n_{pi} and the volume fraction of unfrozen pore liquid n_{pl} can be calculated.

4.3 Thermal properties of mortar

Phase transformation of pore liquid is modelled using the same approach as the external liquid, and thermal properties of mortar are calculated based on the volume fractions of different phases at a specific temperature. Assuming liquid in pores to be pure water, the specific heat capacity of mortar (C_m) is obtained as:

$$C_m = \left(w_{\mathrm{cem,m}} + w_{\mathrm{snd,m}}\right)C_{\mathrm{sm}} + w_{\mathrm{fpl,m}}\frac{\rho_{\mathrm{pl}}S_{\mathrm{pl}}C_{\mathrm{pl}} + \rho_{\mathrm{pi}}S_{\mathrm{pi}}C_{\mathrm{pi}}}{\rho_{\mathrm{pl}}S_{\mathrm{pl}} + \rho_{\mathrm{pi}}S_{\mathrm{pi}}} + w_{\mathrm{fpl,m}}\Delta H\frac{d\alpha_{\mathrm{m,m}}}{dT}$$
$$\alpha_{\mathrm{m,m}} = \frac{1}{2}\frac{\rho_{\mathrm{pl}}n_{\mathrm{pl}} - \rho_{\mathrm{pi}}n_{\mathrm{pi}}}{\rho_{\mathrm{pl}}n_{\mathrm{pl}} + \rho_{\mathrm{pi}}n_{\mathrm{pi}}} \tag{11}$$

where C_{sm} is the specific heat capacity of solid [J/(g.K)] (see Table 4), C_{pl} and C_{pi} are specific heat capacities of unfrozen pore liquid and ice [J/(g.K)], respectively (see Table 1), $\rho_{\mathrm{pl}} = \rho_{\mathrm{dw}}$ is the density of pore liquid [kg/m^3], and $\rho_{\mathrm{pi}} = \rho_{\mathrm{i}}$ is the density of pore ice [kg/m^3].

Thermal conductivity of mortar (k_{m}) is defined as:

$$k_{\mathrm{m}} = \left(n_{\mathrm{cem,m}} + n_{\mathrm{snd,m}}\right)k_{sm} + n_{fpl,m}S_{pl}k_{pl} + n_{fpl,m}S_{pi}k_{pi} \quad (12)$$

where k_{sm}, k_{pl}, and k_{pi} are thermal conductivities of solid (see Table 4), pore liquid and pore ice [W/(m.K)], respectively.

The density of mortar (ρ_{m}) is provided as:

$$\rho_{\mathrm{m}} = \left(n_{\mathrm{cem,m}} + n_{\mathrm{snd,m}}\right)\rho_{\mathrm{sm}} + n_{\mathrm{fpl,m}}S_{\mathrm{pl}}\rho_{\mathrm{pl}} + n_{\mathrm{fpl,m}}S_{\mathrm{pi}}\rho_{\mathrm{pi}} \quad (13)$$

where ρ_{sm} is the density of solid [kg/m^3] (see Table 4).

The properties of solid phase in mortar (calculated for mortar excluding freezable pore liquid) provided in Table 4 and properties provided in Table 1 are used to solve the above equations.

Table 4 – Properties of solid phase in the mortar

Material	ρ [kg/m^3]	C [J/(g.K)]	k [W/(m.K)]
Solid	2468	0.62	3.1

4.4 Validation of Part II

The mortar specimens were cast and saw cut according to the reference method of CEN/TS 12390-9 [16]. The experimental setup and freeze-thaw cycle shown in Figure 2, the shape of the specimen shown in Figure 5, and the temperature control unit described in Section 3.4 were used. However, the temperature control unit applied both cooling and heating using the Peltier element (the built-in heating element was removed), and the feedback sensor was located at the test surface (its location was not well defined in experiments with POM specimen).

Materials and mix design
Mortar specimens were made using cement that was characterized as type CEM I 52.5 N according to EN 197-1 [28], fine aggregates that was CEN Standard sand explained in EN 196-1 [29], and deionized water as mixing water.

The mortar constituents were measured by mass, where the ratio of cement to sand was 1: 3, and the water to cement ratio was 0.45. The mixing procedure provided in EN 196-1 [29] was followed to mix 450 g cement, 1350 g sand, and 202.5 g water for each casting.

Casting and specimen preparation
Figure 5 presents the dimensions of the test specimen, the test surface, and installed thermocouples with sensing points at the central axis of the specimen. To place thermocouples at specific locations in the specimen, holes of 2 mm diameter were drilled in parallel walls of the mould. The sensors were placed through these holes and retained using sticky tape outside the mould. After casting, the top of the mould was sealed to avoid moisture loss, and the mould was placed in a climate room maintained at 20°C for 24 hours. After demolding, the procedure described for the reference method of CEN/TS 12390-9 [16] was followed to prepare the test specimens for the freeze-thaw test.

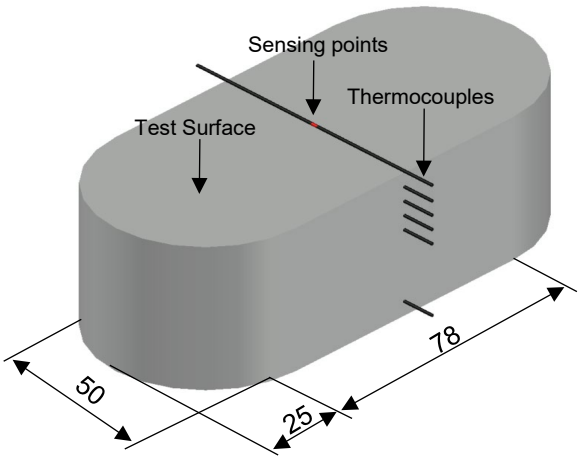

Figure 5 – Schematic figure showing dimensions of the test specimen, the test surface, and installed thermosensors with sensing points at the central axis of the specimen (unit: [mm]).

Boundary conditions for mortar specimens

Table 5 shows the boundary conditions considered for mortar specimens. In addition to the salt concentration and the external liquid layer thickness, the surrounding temperature of the setup is also considered a variable to show its influence on the temperature gradient in mortar. In an experiment ID, "MOR" reflects that it is a mortar specimen. The rest of the ID is similar to the ID for POM specimens, see Section 3.4.

Table 5 – Overview of validation experiments conducted with mortar specimens, and experimentally measured features of the corresponding freezing peaks

Experiment ID	NaCl concentration [%]	Liquid layer thickness [mm]	Surrounding temperature [°C]	Peak start ($T_{\mathrm{sup},\in}$) [°C]	Peak top ($T_{\in,m}$) [°C]
MOR-0s-3mm-20°C	0	3	20	-2.832	-0.061
MOR-3s-3mm-20°C	3	3	20	-4.810	-1.934
MOR-0s-7mm-20°C	0	7	20	-3.233	-0.011
MOR-3s-7mm-20°C	3	7	20	-2.721	-1.145
MOR-0s-3mm-2°C	0	3	2	-2.004	-0.040
MOR-3s-7mm-2°C	3	7	2	-5.514	-1.920

4.5 Results and discussion of porous body

Temperature distributions and freezing peaks for mortars

Figure 6(a) shows a typical development of temperature distribution in mortars considering the boundary conditions in Table 5. The data set providing temperature distribution data for seven freeze-thaw cycles for each experiment in Table 5 can be accessed in Ref. [23]. The simulated temperature distributions for mortar specimens show a good agreement with the experimental temperature distributions when the external liquid layer thickness is 3 mm, whereas the temperature offset after the freezing peak is substantially high when it is 7 mm. The following paragraph provides the possible reasons for this offset in addition to the reasons discussed in Section 3.5.

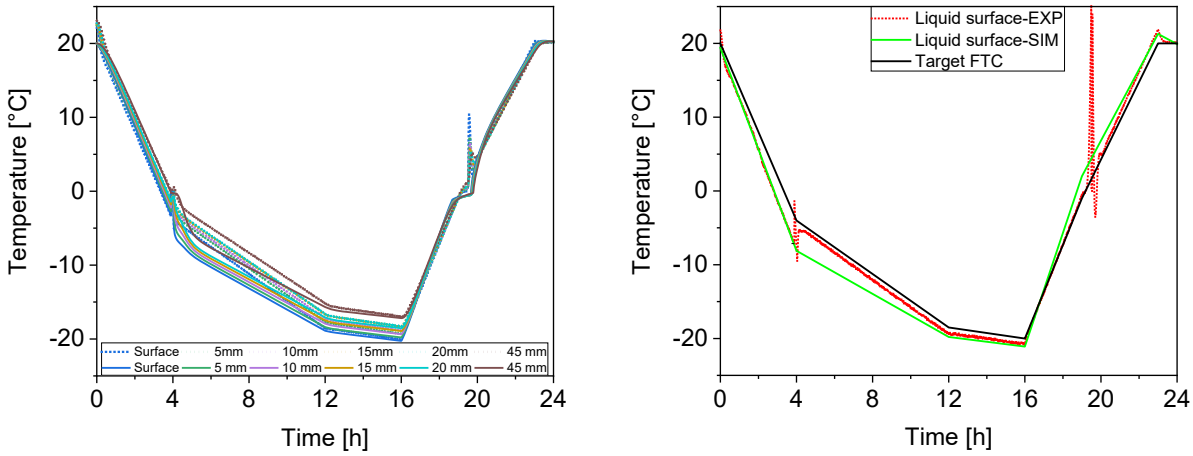

(a) (b)

Figure 6 – (a) Comparison of a typical temperature distribution obtained from simulation (solid lines) and experiment (dotted lines) for mortar specimen, (b) The liquid surface temperature in the experiment (red dotted line) and in the simulation results (green solid line) in reference to the target FTC (black solid line) (obtained from MOR-0s-7mm-20°C).

In experiments for mortar specimens, an additional temperature sensor was placed at the external liquid surface (in liquid) to examine the temperature development at the external liquid surface. Figure 6(b) shows the experimentally measured liquid surface temperature (red dotted line), the liquid surface temperature in simulation (green solid line), and the target FTC to be applied at the test surface (black solid line) for specimen MOR-0s-7mm-20°C. In experiments, the maximum difference between the test surface temperature and the target FTC was 0.3°C. Figure 6(b) shows that the liquid surface temperature in the experiment was identical to the temperature in the simulation at peak start. However, the PID controller applied additional cooling/heating to reach the target FTC as quickly as possible, which was impossible in the simulation. As a result, the liquid surface temperature in the simulation remained much colder than the liquid surface temperature in the experiment resulting in a large temperature offset between the experimental and simulated temperature distribution after the freezing peak.

Figure 7 shows the freezing peaks obtained from simulations (solid lines) and experiments (dash-dotted lines) for mortar specimens. Section 3.5 describes the possible reasons for the observed discrepancies and general behaviour of freezing peaks considering different boundary conditions. However, it is seen in Figures 7 (d) and (f) that a wave-like development starts in experimental curves after the freezing peak (not observed in part I). This is due to the feedback sensor location that is further down compared to its location in part I. The PID controller triggers maximum energy when the temperature difference is largest between setpoint and feedback temperature during the freezing peak. As a result, the temperature exceeds the setpoint. This overshooting continued until the PID controller gradually came back on track. This effect is pronounced for 7 mm thick external liquid compared to 3 mm thick external liquid due to the additional volume of liquid to be heated/cooled.

Important observations have been made from the freezing peaks in Figure 7. In most cases, during the freezing peak, the test surface temperature (blue lines) becomes warmer than the temperature registered 5 mm below the surface (green lines). The Gibbs free energy of the unfrozen liquid is higher than the Gibbs free energy of ice. During this particular period, the Gibbs free energy of unfrozen external liquid can become substantially high due to the increased temperature. A

considerable cryogenic suction where the unfrozen liquid is transported to the ice can take place, causing a significant liquid transport from unfrozen external liquid to the ice in pores of the mortar. Another important observation is the time period where the test surface remained warmer than the temperature registered 5 mm below the test surface. If this period is prolonged, it ensures suitable conditions for cryogenic suction for an extended period. Thus, the longer this period is, the more the cryogenic suction can be.

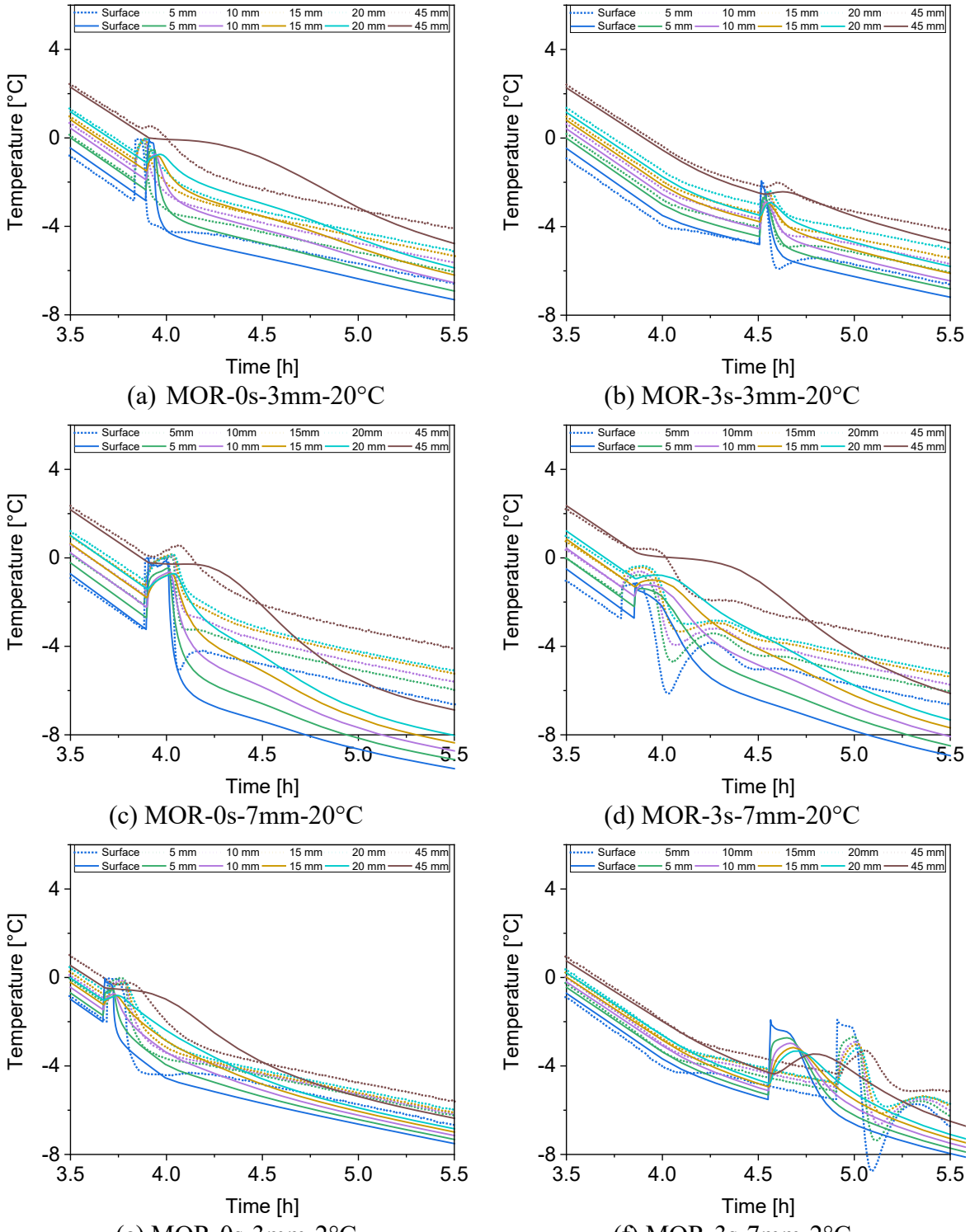

Figure 7 –Freezing peaks obtained from simulations (solid lines) and experiments (dash-dotted lines) for mortar specimens.

The salt concentration, external liquid layer thickness, and surrounding temperature can be considered thermal boundary conditions influencing temperature distribution and thus the extent of frost scaling. The influence of these thermal boundary conditions is discussed below.

Influence of salt concentration
The comparison of Figures 7 (a), (c), and (e) with Figures 7 (b), (d), and (f), respectively, provides the influence of salt concentration of the external liquid on freezing peaks. Since part of 3% NaCl solution remains unfrozen during FTC, the cryogenic suction from the external liquid to ice in frozen pores is possible for a range of freezing temperatures. When external liquid is 3% NaCl solution, substantially more cryogenic suction can occur and result in substantially more scaling compared to when the external liquid is pure water that entirely freezes during the freezing peak.

Influence of external liquid layer thickness
The comparison of Figures 7 (a), (b) with Figures 7 (c) and (d), respectively, provides the influence of the external liquid layer thickness on the freezing peaks. The increase in external liquid layer thickness increases the width of the freezing peak that, in some cases, results in increased frost scaling [7]. In general, the simulated freezing peaks with 7 mm thick external liquid show more discrepancies than 3 mm thick external liquid.

Influence of surrounding temperature
The comparison of Figures 7 (a), (d), with Figures 7 (e) and (f), respectively, provides the influence of the surrounding temperature on the freezing peaks. The temperature curves obtained at different locations appear close to each other when the surrounding temperature is 2°C (Figures 7 (e) and (f)) and further apart from each other when it is 20°C (Figures 7 (a) and (d)). Therefore, the temperature gradient along the depth of mortar is lower when the surrounding temperature is 2°C compared to when it is 20°C. The simulated freezing peaks seem to capture this behaviour.

When ice forms in the vicinity of the test surface, cryogenic suction can, in principle, attract both unfrozen liquid from the external reservoir and from the unfrozen pores below the freezing area. Transport from the lower parts of the specimen is more likely to take place when the temperature gradient is high (i.e. the lower parts are warmer), because then the difference in Gibbs free energy between ice close to the test surface and unfrozen water further away is higher. When the reservoir contains pure water, it entirely freezes during the freezing peak. After this point in time, transport from the reservoir is no longer possible, and ice formation is primarily fed by unfrozen pore liquid.

4.6 Perspective of the model

The present model can simulate the temperature distribution in mortar during freezing and thawing, considering different thermal boundary conditions. The spatial distribution of temperature (perpendicular to the test surface) can be used to determine the spatial distribution of ice and unfrozen liquid, respectively, and Gibbs free energy of the phases at different depths from the test surface, as well as the thermal movement (contraction and expansion) of external ice layer and underlying concrete. Therefore, the present model can serve as a basis for evaluating different freeze-thaw damage mechanisms mentioned in Ref. [2]. For example, the spatial distribution and Gibbs free energy of ice/unfrozen liquid can be used to model the liquid transport and evaluate damage due to cryogenic suction taking place both from the external liquid reservoir and unfrozen pores below the concrete surface to the frozen area near the concrete surface. The spatial distribution of ice/unfrozen liquid can also be used to determine the spatial distribution of hydraulic pressure and thus damage caused by it. Moreover, the thermal movement in the external

ice layer and underlying concrete can be used to evaluate damage due to glue-spall stress that depends on the thermal response mismatch between the external ice layer and underlying concrete. This model may be considered a step towards establishing a virtual laboratory that can mimic the accelerated slat frost scaling test.

5. CONCLUSIONS

Several studies in the literature indicate that some temperature distributions can affect the extent of frost scaling. This study provides aids to simulate temperature distributions considering certain thermal boundary conditions by providing a numerical model that describes the heat transport in freezing mortars when an external liquid reservoir is present on the surface of mortars. The freezing peak that appears when a supercooled liquid transforms into ice is given special attention. The freezing process of the external liquid is modelled in two stages: the recalescence stage that takes supercooling into account and the slow freezing stage taking into account phase transformation and associated latent heat. The boundary conditions considered for simulations include the salt concentration (0% and 3%), the external liquid layer thickness (3 mm and 7 mm), and the surrounding temperature (2°C and 20°C).

The simulated temperature distributions and freezing peaks generally agree with the experimentally measured temperature distributions and freezing peaks, and the model seems to capture the general behaviour (shape) of freezing peaks obtained considering different boundary conditions. However, the temperature boundary used to apply the freeze-thaw cycle caused discrepancies, e.g., a temperature offset appeared after the freezing peak. The modelled supercooling and the following freezing process during the freezing peak are compliant with the experimental observations. The predicted temperature distribution considering certain boundary conditions can be used to explain the cryogenic suction taking place both from the external liquid and unfrozen pores to the freezing vicinity of the test surface and thus the extent of frost scaling.

It is recommended that future studies extending this model replace the temperature boundary used to apply freeze-thaw cycles with a heat flux boundary to avoid the discrepancies caused by the limitations of the temperature boundary. The model is limited to simulating heat transport and thus needs to be extended to take into account coupled heat and moisture transport.

The temperature distribution obtained with this model can be used to determine the spatial distribution of ice and unfrozen liquid, Gibbs free energy of phases at different depths, and the thermal movement of the external ice layer and underlying concrete. This information can be used to evaluate different damage mechanisms and thus improve the understanding of freeze-thaw damage mechanisms.

ACKNOWLEDGMENTS

The present study was made possible due to financial support from several Danish foundations: Larsen & Nielsen Fonden, Martha og Paul Kerrn-Jespersen Fonden, and Aase og Ejnar Danielsens Fond. The authors had valuable discussions with Daniel Eriksson, Ph.D. from KTH Sweden. His suggestions for model building are highly appreciated.

REFERENCES

1. Verbeck G J & Klieger P: "Studies of "Salt" Scaling of Concrete". *Highway Research Board Bulletin*, No. 150, 1957, pp. 1–13.
2. Valenza J.J & Scherer G.W: "A review of salt scaling: II. Mechanisms". *Cement and Concrete Research*, Vol. 37, 2007, pp. 1022–1034.
3. Snyder M.J: "Protective coatings to prevent deterioration of concrete by deicing chemicals". *National cooperative highway research program,* Report 16, Highway Research Board of the Division of Engineering and Industrial Research, National Academy of Sciences - National Research Council, USA, 1965.
4. Lundgreen M & Andalen A: "Round robin test on the freeze-thaw resistance of precast concrete paving blocks". *SP Report* No. 1995:56, Swedish National Testing and Research Institute, Borås, Sweden, 1995.
5. Fabbri A, Coussy O, Fen-Chong T & Monteiro P M J: "Are deicing salts necessary to promote scaling in concrete?". *Journal of Engineering Mechanics*, Vol 134.7, 2008, pp. 589–598.
6. Rosenqvist M, Oxfall M, Fridh K & Hassanzadeh M: "A test method to assess the frost resistance of concrete at the waterline of hydraulic structures". *Materials and Structures*, Vol. 48, 2015, pp. 2403–2415.
7. Hasholt M T: "The importance of boundary conditions in relation to development of frost damage in concrete". *Proceedings,* 73rd RILEM Annual Week & International Conference on Innovative Materials for Sustainable Civil Engineering (IMSCE), Nanjing, China, August 2019, pp. 89–89.
8. Gawin D, Baggio P & Schrefler B A: "Coupled heat water and gas flow in deformable porous media". *International Journal for Numerical Methods in Fluid*, Vol. 20, 1995, pp. 969–987.
9. Coussy O & Monteiro P J M: "Poroelastic model for concrete exposed to freezing temperatures". *Cement and Concrete Research*, Vol. 38, 2008, pp. 40–48.
10. Zuber & Marchand J: "Predicting the volume instability of hydrated cement systems upon freezing using poro-mechanics and local phase equilibria". *Materials and Structures*, Vol. 37, 2004, pp. 257–270.
11. Koniorczyk M, Gawin D, Wieczorek A & Pesavento F: "Concrete frost damage due to cyclic environmental loading—experimental and numerical study". *Proceeding*, Conference on Computational Modelling of Concrete and Concrete Structures, EURO-C, Bad Hofgastein, Austria, 2018, pp. 327–334.
12. Eriksson D, Wahlbom D, Malm R & Fridh K: "Hygro-thermo-mechanical modeling of partially saturated air-entrained concrete containing dissolved salt and exposed to freeze-thaw cycles". *Cement and Concrete Research*, Vol. 141, 2021, 106314.
13. Gong F & Jacobsen S: "Modeling of water transport in highly saturated concrete with wet surface during freeze/thaw". *Cement and Concrete Research*, Vol. 115, 2019, pp. 294–307.
14. Esmaeeli H S, Farnam Y, Bentz D P, Zavattieri P D & Weiss W J: "Numerical simulation of the freeze–thaw behavior of mortar containing deicing salt solution". *Materials and Structures*, Vol. 50, 2017, pp 1–20.
15. Debenedetti P G & Stanley H.E: "Supercooled and Glassy Water". *Physics Today*, Vol. 56, 2003, pp. 40–46.
16. DS/CEN/TS 12390-9:2016: "Testing hardened concrete – Part 9 : Freeze-thaw resistance with de-icing salts – Scaling". Danish Standards Foundation, Nordhavn, Denmark, 2016.
17. Gai S, Peng Z, Moghtaderi B, Yu J & Doroodchi E: "LBM modelling of supercooled water freezing with inclusion of the recalescence stage". *International Journal of Heat and Mass Transfer*, Vol. 146, 2020, 118839.

18. Haynes W M: “CRC Handbook of Chemistry and Physics (Internet Version)”. Taylor and Francis, Boca Raton, Florida, USA, 2016.
19. Pitzer K S, Peiper J C & Busey R.H: “Thermodynamic Properties of Aqueous Sodium Chloride Solutions”. *Journal of Physical and Chemical Reference Data*, Vol. 13, 1984, pp. 1–102.
20. Khattari Y, El Rhafiki T, Choab N, Kousksou T, Alaphilippe M & Zeraouli Y; “Apparent heat capacity method to investigate heat transfer in a composite phase change material”. *Journal of Energy Storage*, Vol. 28, 2020, 101239.
21. Levy F L: “A modified Maxwell-Eucken equation for calculating the thermal conductivity of two-component solutions or mixtures”. *International Journal of Refrigeration*, Vol. 4, 1981, pp. 223–225.
22. C. Therm, TCi Thermal Conductivity Analyzer, Easy MTPS Testing. https://ctherm.com/products/tci-thermal-conductivity-analyzer (accessed May 3, 2021)
23. Faheem A & Hasholt M T: “Data set for article "Numerical modelling of heat transport in freezing mortars with an external liquid reservoir"”. Technical University of Denmark, Kongens Lyngby, Denmark.
24. Faheem A, Ranger M & Hasholt M T: “Developped COMSOL models and other relevant files for article ‘Numerical modelling of heat transport in freezing mortars with an external liquid reservoir’”. Technical University of Denmark, Kongens Lyngby, Denmark, 2021.
25. Powers T C & Brownyard T L: “Studies of the Physical Properties of Hardened Portland Cement Paste”. *ACI Journal Proceedings*, Vol. 43, No. 9, 1946, pp. 249-336.
26. Jensen O M & Hansen P F: “Water-entrained cement-based materials - I. Principles and theoretical background”. *Cement and Concrete Research*, Vol. 31, 2001, pp. 647–654.
27. Zeng Q, Fen-Chong T, Dangla P & Li K: “A study of freezing behavior of cementitious materials by poromechanical approach”. *International Journal of Solids and Structures*, Vol. 48, 2011, pp. 3267–3273.
28. DS/EN 197-1:2011, Cement – Part 1: Composition, specifications and conformity criteria for common cements, Danish Standards Foundation, Nordhavn, Denmark, 2012.
29. DS/EN 196-1, Cement – Part 1: Determination of strength, Danish Standards Foundation, Nordhavn, Denmark, 2016.